

Flight Recorder Localization Following at-Sea Plane Crashes

André Filipe Pereira Rocha
 Instituto Superior Técnico
 Av. Rovisco Pais, 1049-001 Lisboa, Portugal
 andre.p.rocha@ist.utl.pt

Abstract—Recent aircraft disasters over oceans and seas unveiled critical deficiencies in the existing methods of submerged-aircraft localization and recovery. The current localization procedures rely on an acoustic transmitter, denominated Underwater Locator Beacon (ULB), which is attached to the aircraft’s ”black box” and emitting sinusoid-shaped acoustic signals with the purpose of being detected and eventually located by a set of conveniently positioned hydrophones. This paper aims to quantify the precision gains in aircraft localization when some specifications of the currently used beacons are modified, namely its operating frequency, transmitted signal waveform and acoustic power. Moreover, we intend to compare two different source localization algorithms – TOA (Time Of Arrival) and TDOA (Time-Difference Of Arrival) – when applied to this kind of situations. This study is carried out in a simulation environment.

I. INTRODUCTION

The 2009 Air France (AF) flight 447 linking Rio de Janeiro to Paris crashed in the North Atlantic area. French, Brazilian and U.S. authorities took over the wreckage’s search campaigns, which proved unsuccessful as far as finding the aircraft’s Flight Data Recorders (FDR, also known as ”black boxes”) is concerned. The search region was repeatedly acoustically explored in the attempt of detecting the ULB’s transmitted signal, which never happened. It was only in May 2011, almost two years after the crash, that the ULBs were found thanks to the Remora 6000 ROV (Remotely Operated Vehicle).

The ULB is an acoustic transmitter periodically emitting sound waves, as outlined in Fig. 1. Following a crash of an aircraft at the ocean, a search area is laid out based on the information available on the aircraft’s Last Known Position (LKP), which may be derived through flight plan, GPS or radar data. Thus, a set of hydrophone arrays are spread around the aircraft’s expected position, as depicted in Fig. 2.

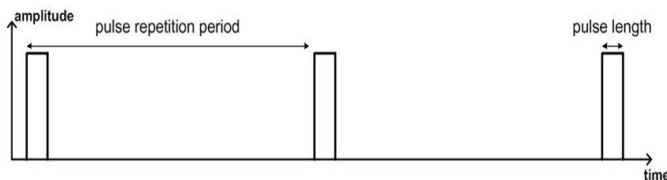


Fig. 1. Periodic sequence of pulses to be transmitted.

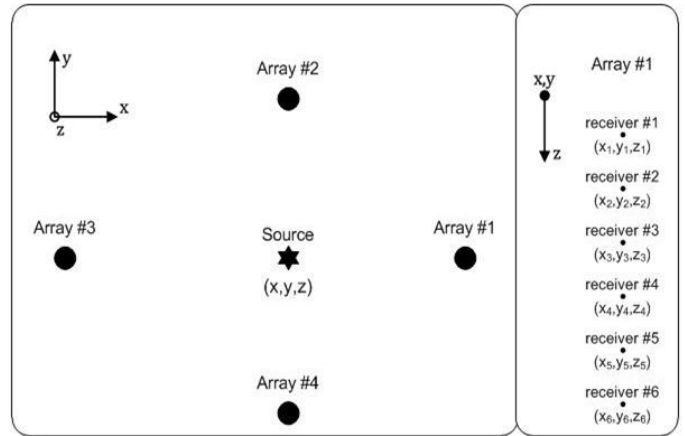


Fig. 2. ULB localization framework.

The AF 447 accident exposed the shortcomings of the current ULB technology. Consequently, we suggest:

- 1) Increasing the autonomy of the ULBs. The current ULB batteries have an operating life of 30 days; increasing it to 90 days would enable longer periods of searching activity, making it more likely to recover the ULBs;
- 2) That the ULBs start transmitting only when interrogated, instead of being water activated. In this sense, the ULBs would be functioning as transponders which could be interrogated by a reference receiver [1], [2], [3]. Again, this would improve the ULBs’ autonomy, as well as allow the determination of the signal’s Round Trip Time (RTT), which in turn yields the ULB-hydrophones distances, essential for the TOA algorithm;
- 3) Decreasing the ULB transmitted signal’s frequency. The attenuation losses induced by the Underwater Acoustic Channel (UAC) are highly dependent on frequency, and increase proportionally to its cube. Hence, reducing the current 37.5 kHz to a reasonable 10 kHz has the potential to greatly enhance the maximum depth and range for which the ULB signal can be detected. The downside of this solution is that the physical size of the beacon would have to increase;
- 4) Substituting the currently used CW (Continuous Wave) sine wave by signals having richer frequency content

and better auto-correlation properties, such as a chirp or a QAM (Quadrature Amplitude Modulation) signal. Thus, the harmful frequency imprecision inherent to the sinusoid tonal is no longer an issue, as broadband signals are easier to reproduce and frequency tune than their CW counterparts. The sine wave's frequency may indeed vary within the 36.5–38.5 kHz interval, albeit its bandwidth is only the inverse of the pulse length (10 ms) – 100 Hz;

- 5) Incorporating in the ULB transmitted signal a digital message conveying valuable data such as the FDR records or the ULB depth, which would greatly aid the search efforts.

This paper is structured as follows. Section II presents the main features of the UAC and its signal distorting agents, and its subsections address the Bellhop simulator and the oceanographic databases used in this work. Section III deals with the signal processing chain, both at the transmitting ULB and the receiving hydrophones, which leads to the determination of the signal's RTT. Section IV addresses the source localization algorithms TOA and TDOA, whereas section V presents the simulation results obtained.

Remark: The material exposition is made to handle discrete-time signals. The Nyquist theorem states that there is no loss of information when converting a continuous-time signal to discrete-time if the sampling rate is sufficiently high.

II. UNDERWATER ACOUSTIC CHANNEL

Conceptually, the underwater communication problem is described in Fig. 3:

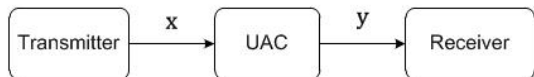


Fig. 3. Underwater communication problem.

The ocean is an acoustic waveguide limited above by the sea surface and below by the sea floor. Sound waves at middle and high frequencies (> 5 kHz) can be fairly modelled as propagating along paths or rays through the ocean. In an ideal homogeneous environment the ray paths would follow straight lines radiating from the source and eventually reaching the receiver [5]; in the real ocean environment, the ray paths follow curvilinear lines due to the high variability of the Sound Speed Profile (SSP), which induces a bending of the sound rays towards regions of low sound speed (refraction). Additionally, it is verified that the acoustic beams are reflected at both the sea surface and the sea bottom.

Scattering Loss: The reflection of sound at both ocean interfaces causes a partial loss in its acoustic energy. Thus, the energy that is scattered in a direction other than the direction of the receiver is effectively lost. Furthermore, the field scattered away from the specular direction and, in particular, the backscattered field (reverberation) acts as negative interference for the main field.

Absorption Loss: Seawater and sea floor absorption is a sound attenuating mechanism consisting of the conversion of the acoustic energy of sound waves into another form of energy, which is then retained by the lossy agent. Sea floor sound-absorption occurs because the reflection of energy is incomplete, and sound penetrates into the bottom. The absorption of sound by the water is highly dependent on frequency, meaning that high frequency signals are far more attenuated than low frequency ones, as evidenced by (1), where α_w denotes the seawater attenuation.

$$\alpha_w = 3.3 \times 10^{-3} + \frac{0.11f^2}{1 + f^2} + \frac{44f^2}{4100f + f^2} + 3 \times 10^{-4}f^2 \quad (1)$$

Spreading Loss: The spreading loss is simply a measure of the signal weakening as it propagates outward from the source. In regions close from the emitter, the acoustic wavefront radiates spherically, and the signal intensity is inversely proportional to the surface of the sphere: $I \propto \frac{1}{4\pi R^2}$, where R is the sphere radius. The spherical spreading in the nearfield is followed by a transition region towards cylindrical spreading in the farfield, where the sound intensity becomes inversely proportional to the surface of a cylinder of radius R and depth D : $I \propto \frac{1}{2\pi RD}$.

Multipath propagation is a very critical aspect of sound propagation in the ocean, which results in acoustic signals travelling from the transmitter to the receivers by two or more different paths (hundreds even), as exemplified in Fig. 4.

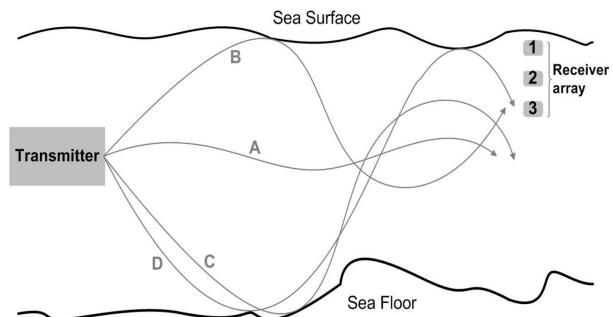


Fig. 4. Multipath propagation. A – direct path; B – surface-reflected path; C – bottom-reflected path; D – bottom-reflected surface-reflected path.

The multipath phenomenon is characterized by the input delay-spread function g , which reflects not only the energy losses endured by each path connecting the emitter to the receiver, but also the delay-spread pattern obtained at the receiver. Fig. 5 presents the signal arrival profile at each receiver for the situation of Fig. 4. From Fig. 5 it is immediate to understand that g resembles a train of Dirac impulses:

$$g[n] = \sum_{l=1}^L a_l \delta(n - N_l), \quad (2)$$

where L is the number of incoming rays at the receiver, a_l is the l^{th} ray amplitude and N_l is the corresponding time

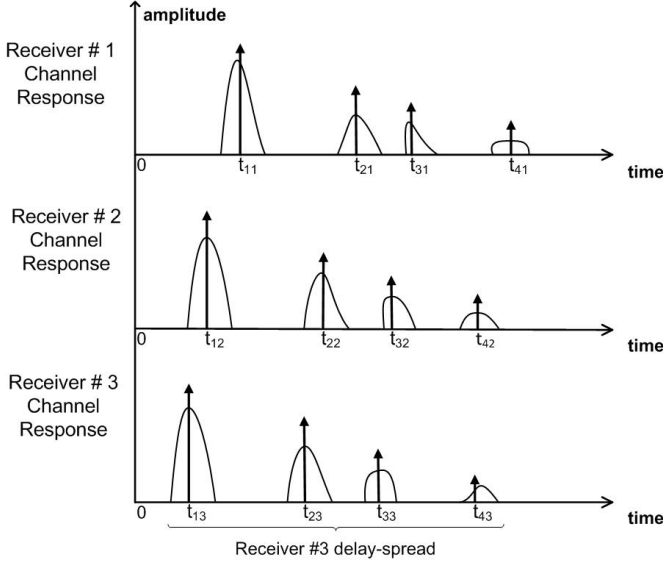


Fig. 5. Delay-spread pattern for the situation depicted in Fig. 4.

delay (in discrete-time). The ray amplitudes a_l are a measure of the absorption, scattering and spreading losses of the ocean environment.

In underwater acoustic communications, ambient noise is also an issue because it masks the signal of interest. The several different sources of noise in the ocean are generally grouped into four categories: turbulence (t), waves (w), thermal (th) and shipping noise (s). The ocean noise is then characterized as a Gaussian variable having a Power Spectral Density (PSD) resulting from four different contributions:

$$N(f) = N_t(f) + N_w(f) + N_{th}(f) + N_s(f), \quad (3)$$

where

$$10 \log_{10} N_t(f) = 17 - 30 \log_{10} f \quad (4)$$

$$10 \log_{10} N_w(f) = 50 + 7.5w^{\frac{1}{2}} + 20 \log_{10} f - 40 \log_{10}(f + 0.4) \quad (5)$$

$$10 \log_{10} N_{th}(f) = -15 + 20 \log_{10} f \quad (6)$$

$$10 \log_{10} N_s(f) = 40 + 20(s - 0.5) + 26 \log_{10} f - 60 \log_{10}(f + 0.03). \quad (7)$$

These formulas were taken from [7] and present the noise power N in $\text{dB re } 1\mu\text{Pa Hz}^{-1}$ as a function of the acoustic frequency f in kHz. Along these lines, the received signal y can be decomposed in two terms, one denoting the contribution of the multipath attenuating effects (y_m) and the other expressing the influence of underwater noise (y_n):

$$y[n] = y_m[n] + y_n[n], \quad (8)$$

where

$$y_m[n] = x[n] \star g[n] = g[n] \star x[n] = \sum_{k=-\infty}^{\infty} \left[\sum_{l=1}^L a_l \delta(k - N_l) \right] x(n - k). \quad (9)$$

The term $y_m[n]$ is a time-delayed and amplitude-attenuated version of the transmitted signal $x[n]$.

A. Bellhop

Bellhop is a freely distributed ray-tracing code incorporated in the Acoustic Toolbox (check [11]). An exhaustive description of this acoustic model, including a detailed theoretical study of the wave theory behind it, is presented in [8]. Bellhop is designed in order to perform two-dimensional acoustic ray tracing for a given SSP or a given sound speed field, in ocean waveguides with flat or variable absorbing boundaries [12]. Output options include ray coordinates, travel time, amplitude, eigenrays, acoustic pressure or transmission loss (either coherent, incoherent or semi-coherent).

Thus, we use Bellhop to simulate the time-delaying and amplitude-attenuating effects of the UAC on the transmitted signal x . Three input files are required: a main environmental file setting the simulation scenario for the localization problem (source depth, receivers' depths and ranges, signal frequency, etc.), a file describing the bathymetric profile, and a bottom reflection coefficient file generated through a Bounce run. Bounce is a program also incorporated in the Acoustic Toolbox, and computes the reflection coefficient if given an adequate input.

B. Geoacoustic Database

A geoacoustic database is needed in this work to obtain the data which serves as input to Bellhop's (and Bounce's) simulations. Thus, we resort to the GEBCO (General Bathymetric Chart of the Oceans) bathymetric database of the world's oceans, adopt the World Ocean Atlas 2009 material on SSPs, and utilize the DECK 41 bottom sediments database.

III. DELAY ESTIMATION

The state-of-the-art system depends on the directionality of the receiving hydrophones to estimate the ULB's position via a combination of AOA (Angle Of Arrival) and RSS (Received Signal Strength) algorithms. In this work we have to estimate the ULB-hydrophones distances to apply our methods of interest – TOA and TDOA. Thus, the reference receiver interrogates the transponder-acting ULB to synchronize clocks, setting the reference time origin. Once interrogated, the ULB starts transmitting the acoustic signal to be detected and treated by the hydrophones to determine its RTT, which in turn yields the emitter-receiver distances.

A. Transmitter

The transmitter architecture is depicted in Fig. 6.

The generator produces the wave signal in baseband, defining all the significant signal characteristics, such as its waveform, nominal frequency or bandwidth B_s . In this study, we

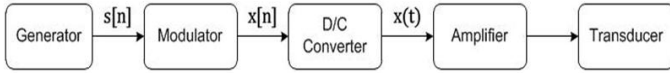


Fig. 6. Transmitter block.

employ four different types of signals: the state-of-the-art high uncertain frequency sine wave and, on the other hand, sinusoid, chirp and QAM-4 signals with lower carrier frequency. Then, the baseband signal s is frequency-shifted by a modulating carrier of frequency f_c , creating the passband signal x , in accordance with (10), where ω_c is the carrier's angular frequency and ϕ is the phase offset of the transmitter's carrier. In this way, if we want to transmit a signal with frequency f_0 , the generated signal s must have a frequency $f_0 - f_c$ so that when modulated its frequency becomes $(f_0 - f_c) + f_c = f_0$. This frequency spectrum shift is exemplified in Fig. 7.

$$x[n] = s[n] \text{Re}\{e^{j(\omega_c n + \phi)}\} \quad (10)$$

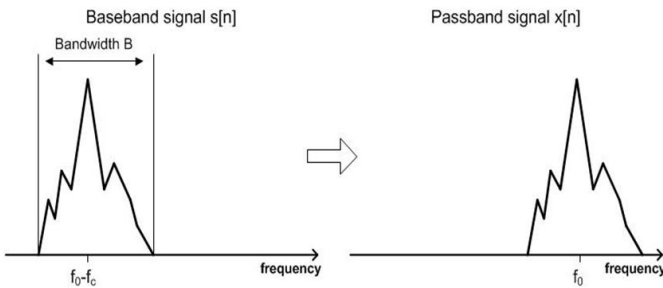


Fig. 7. Frequency spectrum shift resulting from the modulation process. The baseband signal presents lower frequencies than the passband signal.

After exiting the modulator, the discrete-time signal $x[n]$ goes through the D/C converter where it is transformed into its continuous-time equivalent $x(t)$, at a sampling frequency f_s . Thereafter, the amplifier amplifies the continuous-time modulated signal and drives the transducer to produce sound waves, which are subsequently broadcast through the UAC. The discrete-time sinusoid transmitted signal is defined as

$$x_s[n] = A \sin(2\pi f_0 n + \varphi), \quad (11)$$

where A is the amplitude and φ is the initial phase, or phase offset, in radians.

The discrete-time chirp transmitted signal is

$$x_c[n] = A \cos\left(\left(\omega_0 + \frac{1}{2}\beta n\right)n + \varphi\right), \quad (12)$$

where β is the frequency variation rate.

The discrete-time QAM-4 transmitted signal is defined as

$$x_{qam}[n] = I[n] \cos(2\pi f_c n) + Q[n] \sin(2\pi f_c n). \quad (13)$$

The QAM digital modulation architecture conveys two digital symbol streams by changing the amplitudes of two carrier waves using the ASK/PSK scheme. The two carrier sinusoids are out of phase with each other by 90° and are thereby quadrature carriers of quadrature components. The modulated waves are summed and the resulting waveform is a combination of both the PSK (Phase Shift-Keying) and the ASK (Amplitude Shift-Keying) modulations. $I[n]$ and $Q[n]$ are the two symbol streams to be transmitted. The in-phase symbol stream is obtained as

$$I[n] = \sum_k a_k p(n - kN), \quad (14)$$

where a_k is the amplitude of symbol k , p is the shape of the signalling pulses (root-raised-cosine [13], in this case), and N is the number of samples per symbol interval. The quadrature sequence $Q[n]$ is generated similarly. In the case of a digital quaternary modulation, as QAM-4, each symbol is constituted by a combination of 4 bits (2^4 [bits] encode 1 of 16 [symbols]). The most significant parameters of each of the interest signals are gathered next:

	Sine	Chirp	QAM-4	SA sine
Pulse length τ (ms)	50	50	50	10
Pulse repetition period T_p (s)	1.0	1.0	1.0	1.0
Signal frequency f_0 (kHz)	10	10	10	37.5
Signal bandwidth B_s	$\frac{1}{\tau}$	2 kHz	2 kHz	$\frac{1}{\tau}$
Carrier frequency f_c (kHz)	10	10	10	37.5
Sampling frequency f_s (kHz)	50	50	50	85

TABLE I
CHARACTERISTICS OF EACH OF THE POSSIBLE TRANSMITTED SIGNALS: SINE, CHIRP, QAM AND STATE-OF-THE-ART SINE.

B. Receiver

The state-of-the-art system's receiver is pictured in Fig. 8, whereas the proposed receiver structure is outlined in Fig. 9.

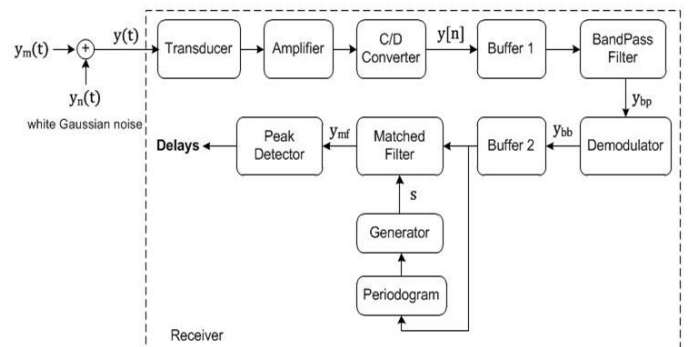


Fig. 8. Receiver configuration when the state-of-the-art signal (sine) is transmitted.

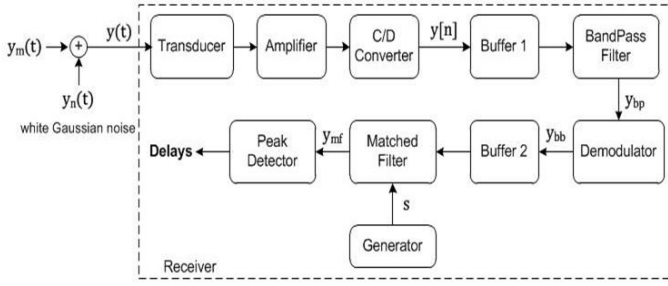


Fig. 9. Receiver conformation when the alternative signals (sine, chirp, QAM) are transmitted.

The ensemble [transducer + C/D converter] converts the analog acoustic signal to a discrete-time version of the received signal.

The bandpass filter is essential in partially removing the disturbances of the ocean ambient noise. Its goal is to filter the received signal so that only the transmitted passband signal's frequency band remains. Ergo, the bandpass filter has a bandwidth of 2 kHz when the SA sine, chirp and QAM signals are employed, and 300 Hz for the sinusoid case. Unlike the straightforward filter bandwidths of the chirp and QAM signals, the other cases have to be explained. Although the sinusoid filter bandwidth should be 20 Hz (from Table I), a filter with such a narrow bandwidth is difficult to realize in practice, so a reasonable 300 Hz bandwidth is chosen. As for the SA sine filter bandwidth, it has to be 2 kHz to cover the frequency uncertainty associated with the SA sine, whose frequency is only known to vary in a 2 kHz band around the central frequency of 37.5 kHz. Consequently, there is a decrease in the receiver performance since the tolerated noise power unnecessarily increases. Note that a linear phase FIR (Finite Impulse Response) filter is preferred over an IIR (Infinite Impulse Response) filter so that there is no signal distortion due to the time delay of frequencies relative to one another. The filter order is 100 for the chirp and QAM signals, 144 in the SA sine case and 566 for the sinusoid.

The demodulator block is detailed in Fig. 10. The demodulator must not only frequency-shift the received signal back to baseband, but also make up for the unknown phase delay ϕ between the transmitter's and the receiver's carriers.

Subsequently, the signal enters the matched filter which consists of correlating the received signal with an exact replica of the transmitted signal. The purpose of this cross-correlation function is to detect the transmitted signal amongst the ocean noise. Thus, refer to Fig. 11 to understand that the correlation of a sinusoid with a sinusoid, called auto-correlation, yields a unique function with a high peak, unlike the cross-correlation of a sinusoid with noise. The auto-correlation functions of the sine, chirp and QAM signals can be compared in Fig. 12.

In the SA system, the receiver replica of the transmitted signal is not so accurate due to the frequency imprecision. Because the receiver is not aware of the transmitted signal's

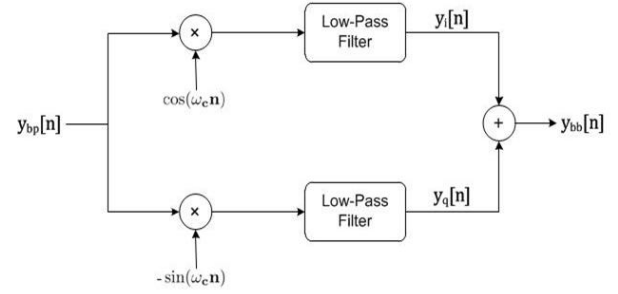


Fig. 10. Demodulator block.

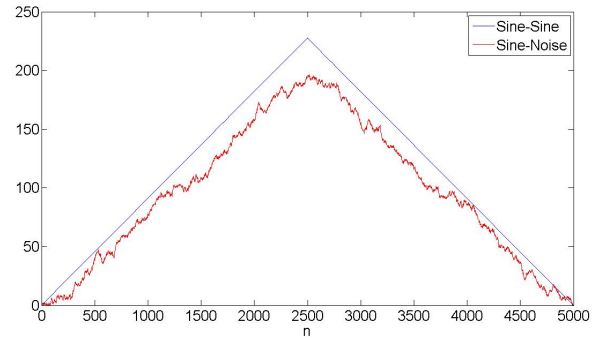


Fig. 11. Sinusoid auto-correlation function, and sinusoid-noise cross-correlation function.

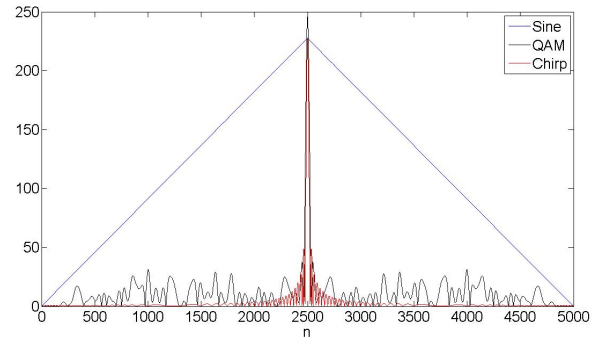


Fig. 12. Sinusoid, chirp and QAM auto-correlation functions.

frequency, it has to estimate it thanks to the periodogram of the received signal, which results in further inaccuracies in the delay estimation process. The periodogram of a signal is an estimate of its spectral density.

The peak detector decides that there is signal present if the maximum of the correlation function exceeds a pre-defined threshold. In this sense, it is verified that the QAM and chirp auto-correlation functions perform better than the sinusoid one, as they possess higher peaks. Once the peak detector measures a peak above the threshold, the ULB signal is detected, and its time delay is the sample number N_{peak} at which the strongest peak occurred. Therefore, the transmitter-reference-receiver distance can be determined as

$$r_{ref} = \frac{t_{peak_{ref}}}{2}c = \frac{N_{peak_{ref}}}{2f_s}c, \quad (15)$$

whereas the remaining transmitter-receivers distances are computed as

$$r = \frac{t_{peak} - \frac{t_{peak_{ref}}}{2}}{2}c = \frac{N_{peak} - \frac{N_{peak_{ref}}}{2}}{2f_s}c. \quad (16)$$

IV. SOURCE LOCALIZATION

Before presenting the localization algorithms, it is convenient to clarify the notation for this section: scalar values are represented by lowercase letters (example: x), vectors are represented by boldface lowercase letters (example: \mathbf{x}), matrices are represented by boldface uppercase letters (example: \mathbf{A}), the identity matrix of order n is denoted by \mathbf{I}_n , the all-zero matrix of order $n \times k$ is designated by $\mathbf{0}_{n \times k}$, the transpose of a matrix \mathbf{H} is referred to as \mathbf{H}^T , and the inverse of a matrix \mathbf{H} is denoted by \mathbf{H}^{-1} . Moreover, given a positive definite $n \times n$ matrix \mathbf{B} and a symmetric $n \times n$ matrix \mathbf{A} , the generalized eigenvalues of the matrix pair (\mathbf{A}, \mathbf{B}) are denoted by λ_i , $i = 1, \dots, n$.

Fig. 2 illustrates the source localization problems framework. The unknown source's coordinate vector is $\mathbf{x} = [x \ y \ z]^T$, and coordinates of the i^{th} receiver are expressed as $\mathbf{a}_i = [x_i \ y_i \ z_i]^T$, $i = 1, \dots, m$, where m is the number of receivers distributed by k arrays. The next subsections present the work in [10].

A. TOA Algorithm

The TOA source localization algorithm consists of estimating \mathbf{x} from the measured source-receiver distances r_i , which can be expressed as

$$r_i = \|\mathbf{x} - \mathbf{a}_i\| + \epsilon_i, \quad i = 1, \dots, m, \quad (17)$$

where ϵ_i stands for the error between the true source-receiver distance and the measured one at the i^{th} receiver. We resort to the SR-LS (Squared-Range-based Least Squares) methodology to estimate the source's position. Thus, we want to minimize the following cost function:

$$\underset{\mathbf{x}}{\text{minimize}} \quad \sum_{i=1}^m (\|\mathbf{x} - \mathbf{a}_i\|^2 - r_i^2)^2. \quad (18)$$

Although it is nonconvex, the SR-LS cost function is shown to have a global optimal solution that can be efficiently computed. First, let us transform (18) into a constrained minimization problem:

$$\underset{\mathbf{x} \in \mathbb{R}^n, \alpha \in \mathbb{R}}{\text{minimize}} \quad \left\{ \begin{array}{l} \sum_{i=1}^m (\alpha - \mathbf{a}_i^T \mathbf{x} + \|\mathbf{a}_i\|^2 - r_i^2)^2 : \\ \|\mathbf{x}\|^2 = \alpha \end{array} \right\}. \quad (19)$$

In (19) n is the dimension of the ambient space, naturally 3 in this case. Using $\mathbf{y} = [\mathbf{x}^T, \alpha]^T$, (19) can be rewritten in matrix form as

$$\underset{\mathbf{y} \in \mathbb{R}^{n+1}}{\text{minimize}} \quad \left\{ \|\mathbf{A}\mathbf{y} - \mathbf{b}\|^2 : \mathbf{y}^T \mathbf{D}\mathbf{y} + 2\mathbf{f}^T \mathbf{y} = 0 \right\}, \quad (20)$$

where

$$\mathbf{A} = \begin{bmatrix} -2\mathbf{a}_1^T & 1 \\ \vdots & \vdots \\ -2\mathbf{a}_m^T & 1 \end{bmatrix} \quad (21)$$

$$\mathbf{b} = \begin{bmatrix} r_1^2 - \|\mathbf{a}_1\|^2 \\ \vdots \\ r_m^2 - \|\mathbf{a}_m\|^2 \end{bmatrix} \quad (22)$$

$$\mathbf{D} = \begin{bmatrix} \mathbf{I}_n & \mathbf{0}_{n \times 1} \\ \mathbf{0}_{1 \times n} & 0 \end{bmatrix} \quad (23)$$

$$\mathbf{f} = \begin{bmatrix} \mathbf{0}_{n \times 1} \\ 0.5 \end{bmatrix}. \quad (24)$$

The cost function of (20) fits the Generalized Trust Region Subproblems (GTRS) description, since it consists of minimizing a quadratic function subject to a single quadratic constraint. In [10] and the references therein it is shown that the optimal solution of (20) is $\hat{\mathbf{y}} \in \mathbb{R}^{n+1}$ such that

$$\hat{\mathbf{y}}(\lambda) = (\mathbf{A}^T \mathbf{A} + \lambda \mathbf{D})^{-1} (\mathbf{A}^T \mathbf{b} - \lambda \mathbf{f}), \quad (25)$$

where λ is obtained through

$$\varphi(\lambda) \equiv \hat{\mathbf{y}}(\lambda)^T \mathbf{D} \hat{\mathbf{y}}(\lambda) + 2\mathbf{f}^T \hat{\mathbf{y}}(\lambda) = 0, \quad \lambda \in I. \quad (26)$$

The interval I consists of all λ for which $\mathbf{A}^T \mathbf{A} + \lambda \mathbf{D}$ is positive definite, which immediately implies that

$$I = \left(-\frac{1}{\lambda_1(\mathbf{D}, \mathbf{A}^T \mathbf{A})}, \infty \right). \quad (27)$$

The SR-LS estimate of the source's position is given by the first n components of the solution vector $\hat{\mathbf{y}}$ in (25).

B. TDOA Algorithm

The TDOA method estimates the source's position based on the receivers' positions and the distance-difference measurements, which can be written as

$$d_i = \|\mathbf{x} - \mathbf{a}'_i\| - \|\mathbf{x}\|, \quad i = 1, \dots, m, \quad (28)$$

which, when squared, yields the following equation in the vector \mathbf{x} :

$$-2d_i \|\mathbf{x}\| - 2\mathbf{a}'_i{}^T \mathbf{x} = d_i^2 - \|\mathbf{a}'_i\|^2, \quad i = 1, \dots, m, \quad (29)$$

where \mathbf{a}'_i denotes the i^{th} receiver position in the reference-receiver-centred coordinate frame (reference receiver located

at the origin). Thus, a reasonable way to estimate x is via the minimization of the SRD-LS (Squared-Range-Difference-based Least Squares) criterion

$$\underset{\mathbf{x} \in \mathbb{R}^n}{\text{minimize}} \sum_{i=1}^m (-2\mathbf{a}'_i{}^T \mathbf{x} - 2d_i \|\mathbf{x}\| - g_i)^2, \quad (30)$$

where $g_i = d_i^2 - \|\mathbf{a}'_i\|^2$. Reformulating (30) as a constrained LS problem with $\mathbf{y} = [\mathbf{x}^T, \|\mathbf{x}\|]^T$:

$$\underset{\mathbf{y} \in \mathbb{R}^{n+1}}{\text{minimize}} \{ \|\mathbf{B}\mathbf{y} - \mathbf{g}\|^2 : \mathbf{y}^T \mathbf{C}\mathbf{y} = 0, y_{n+1} \geq 0 \}, \quad (31)$$

where

$$\mathbf{B} = \begin{bmatrix} -2\mathbf{a}'_1{}^T & -2d_1 \\ \vdots & \vdots \\ -2\mathbf{a}'_m{}^T & -2d_m \end{bmatrix} \quad (32)$$

$$\mathbf{C} = \begin{bmatrix} \mathbf{I}_n & \mathbf{0}_{n \times 1} \\ \mathbf{0}_{1 \times n} & -1 \end{bmatrix}. \quad (33)$$

It is proved in [10] that $\mathbf{z} \in \mathbb{R}^{n+1}$ is an optimal solution of (31):

$$\mathbf{z} \equiv \tilde{\mathbf{y}}(\lambda) = (\mathbf{B}^T \mathbf{B} + \lambda \mathbf{C})^{-1} \mathbf{B}^T \mathbf{g}, \quad (34)$$

where λ is determined as

$$\tilde{\mathbf{y}}^T \mathbf{C} \tilde{\mathbf{y}} = 0. \quad (35)$$

If \mathbf{z} satisfies the condition $z_{n+1} \geq 0$, then \mathbf{z} is a global optimal solution of (31). Otherwise, one needs to find all roots $\lambda_1, \dots, \lambda_p$ of

$$\tilde{\mathbf{y}}^T(\lambda) \mathbf{C} \tilde{\mathbf{y}}(\lambda) = 0, \quad \lambda \in I_0 \cup I_2 \quad (36)$$

for which the $(n+1)$ th component of $\tilde{\mathbf{y}}(\lambda_i)$ is non-negative. The intervals are found by

$$I_0 = (\alpha_0, \infty) \quad (37)$$

$$I_2 = (\alpha_2, \alpha_1), \quad (38)$$

where

$$\alpha_i = -\frac{1}{\lambda_i(\mathbf{C}, \mathbf{B}^T \mathbf{B})} \quad i = 1, \dots, n \quad (39)$$

$$\alpha_0 = -\frac{1}{\lambda_{n+1}(\mathbf{C}, \mathbf{B}^T \mathbf{B})}. \quad (40)$$

Then, the solution of the SRD-LS problem are the first n components of \mathbf{z} , which is the vector with the smallest objective function among the vectors $\mathbf{0}, \tilde{\mathbf{y}}(\lambda_1), \dots, \tilde{\mathbf{y}}(\lambda_p)$.

V. SIMULATION RESULTS

A. Scenarios

The simulation results were obtained for three different localization setups. These localization scenarios are rather deterministic instead of being random or stochastic. This is inherently due to the nature of the crashed-aircraft localization issue: there is a well-defined search radius and coordinated operation of search vessels around the wreckage's expected position.

Along these lines, three topologies are defined:

- 1) **Scenario 1**: 4 receiving arrays, each composed by 10 hydrophones, are symmetrically spread around the source, as sketched in Fig. 13;
- 2) **Scenario 2**: 4 receiving arrays, each composed by 10 hydrophones, are spread around the source in a non-symmetrical fashion, as laid out in Fig. 14;
- 3) **Scenario 3**: 4 receiving arrays, each composed by 10 hydrophones, are spread in a non-efficient way since the source does not lie inside the convex hull, as depicted in Fig. 15.

All of these cases are characterized by a high depth discrepancy between the source and the receivers as they are located at the sea floor and the sea surface, respectively.

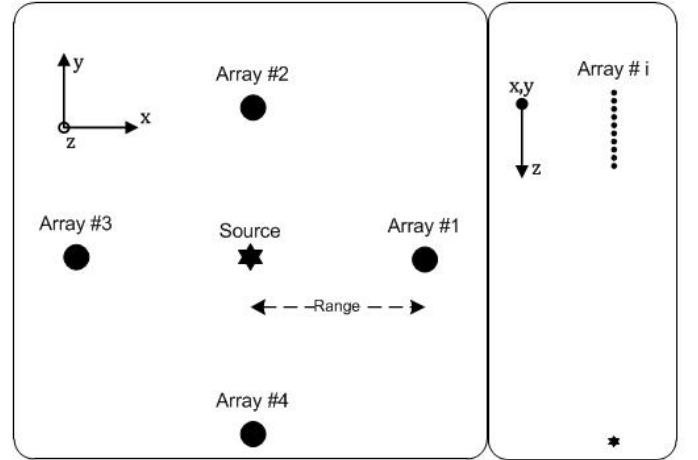


Fig. 13. Localization scenario 1.

B. Range Estimation

The range estimation algorithms are evaluated resorting to the localization scenario 1. In this manner, it is easy to check how the transmitter-hydrophone distance affects the observations. As the transmitter-receiver distances vary, the signal-to-noise ratio at the receivers vary accordingly, ergo the measured distances evolution with the SNR at the receiver is inherently obtained.

The errors presented in Figs. 16 and 17 are the mean of the resulting errors for the 4 arrays, and are given in absolute and relative values, respectively. The estimated ranges deviate from the real transmitter-receiver distances due to two reasons:

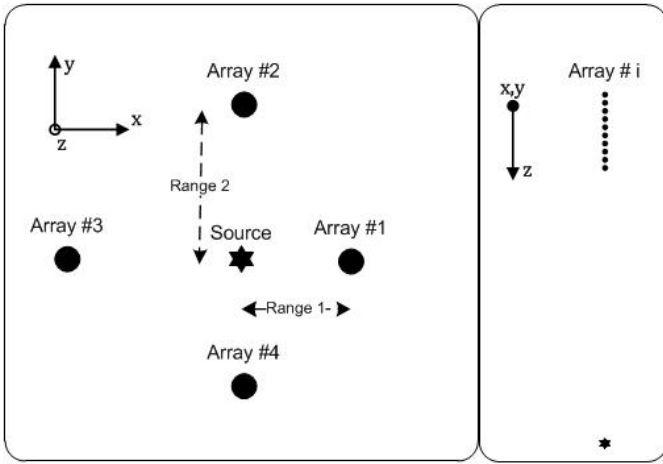


Fig. 14. Localization scenario 2.

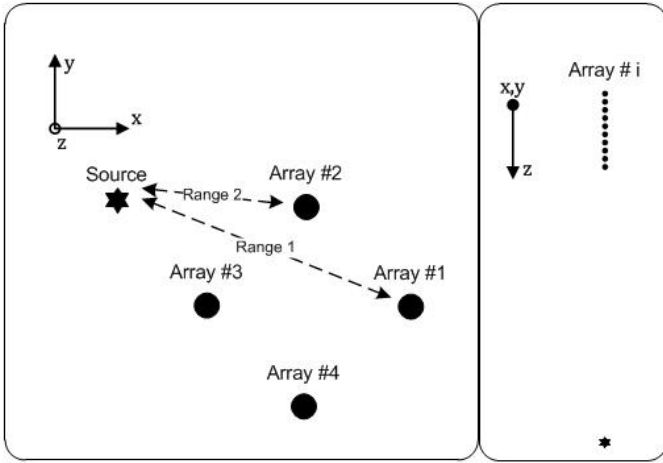


Fig. 15. Localization scenario 3.

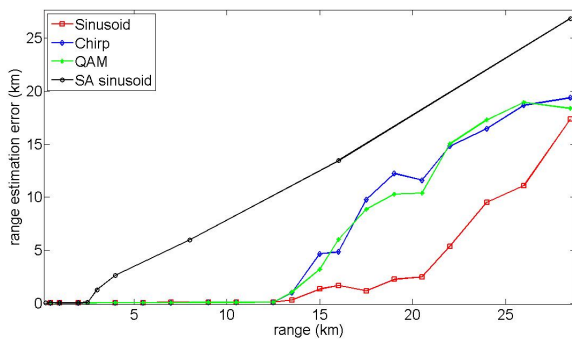


Fig. 16. Range estimation error as a function of the ULB-hydrophone distance.

- 1) The ray paths do not follow straight lines from the emitter to the receiver – the curvilinear ray trajectories are longer than the rectilinear transmitter-receiver distance;
- 2) The receiving apparatus is not perfect, and therefore the noise introduced by the UAC will cause the receivers

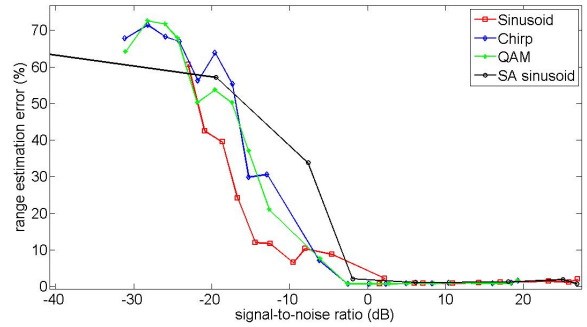


Fig. 17. Range estimation error as a function of the SNR at the receiver.

to calculate the distances with a certain imprecision. In fact, it is verified that the distance pattern measured within an array is non-coherent; an example of this non-coherence is a deeper hydrophone measuring a higher distance than a shallower one.

In this fashion, it is easy to understand the presented graphs. The range-error increases with increasing range because the distance-difference between the curvilinear and the rectilinear lines connecting the ULB to the hydrophones increases, and the signal-to-noise ratio decreases. Furthermore, it is seen that there is a threshold transmitter-receiver distance and signal-to-noise ratio up to which the ranges are reasonably estimated. Once that threshold is crossed, the error quickly increases with the ULB-hydrophone distance.

Naturally, the state-of-the-art system performs much worse than the alternatives: increasing the transmitter-receiver distance past 3 km severely deteriorates the estimated ranges' precision for the SA sine, whereas this threshold is approximately 13 km for the remaining signals. Thus, the maximum ULB-hydrophone range for which detection is accomplished is enhanced by 10 km.

Based on Fig. 17, acknowledge that the error evolution with the SNR is approximately equal for all the signals. Thus, it is verified that the SNR decreases much faster with the emitter-receiver range when the SA sine is employed, due to its high frequency. On the other hand, the sinusoid performance with the ULB-hydrophone distance is better than the other signals' because of its bandpass filter's narrow bandwidth (300 Hz), contrasting with the 2 kHz bandwidth of the chirp and QAM signals. Hence, the sinusoid's bandpass filter best limits the received noise power.

C. Source Localization

Topologies 2 and 3 were chosen to perform the source localization study because they are in theory more complicated than scenario 1. Therefore, if the localization algorithms show a good behavior for these scenarios, then topology 1 should be no problem. The localization errors in the graphics of Figs. 18 to 22 are the norm of the absolute error vector.

The localization scenario 2 is used to compute the localization error versus the size of the convex hull. That is the maximum array-source range in a given situation. The arrays' distances

to the ULB differ 800 m between consecutive arrays; referring to Fig. 14, this means that if range 1 equals e.g. 6 km, then range 2 is 5.2 km, range 3 is 4.4 km and range 4 equals 3.6 km. When the dimension of the convex hull increases, it means that the farthest array's distance to the emitter increases, and the other arrays' ranges increase accordingly.

Topology 3 is used to evaluate the influence of the ULB source level on the localization error. In this problem, the arrays are fixed at coordinates $\mathbf{a}_i = [13500 \ 2500 \ z_i]^T$, $i = 1, \dots, 10$ (array 1), $\mathbf{a}_i = [7500 \ 8500 \ z_i]^T$, $i = 11, \dots, 20$ (array 2), $\mathbf{a}_i = [1500 \ 2500 \ z_i]^T$, $i = 21, \dots, 30$ (array 3) and $\mathbf{a}_i = [7500 \ -3500 \ z_i]^T$, $i = 31, \dots, 40$ (array 4). Recall that the source is placed at $\mathbf{x} = [0 \ 0 \ 2296]^T$, and the depths z_i vary between 6 m and 42 m. Array 1 is the farthest from the source, being located at approximately 14 km from it.

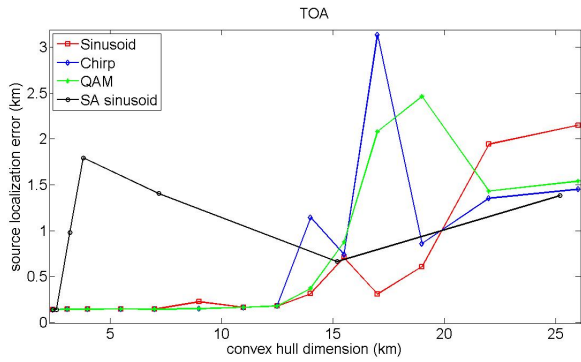


Fig. 18. TOA source localization error as a function of the dimension of the receiving convex hull (topology 2). There is an increase of the TOA source localization error with increasing convex hull size.

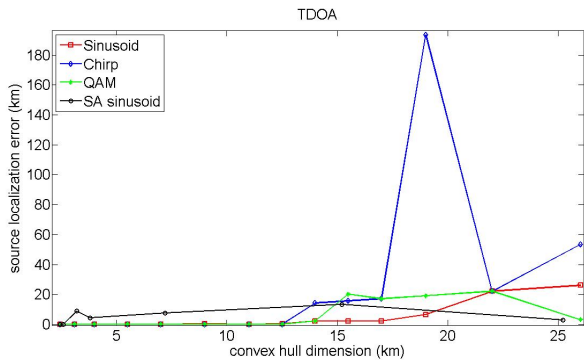


Fig. 19. TDOA source localization error as a function of the dimension of the receiving convex hull (topology 2). There is an increase of the TDOA source localization error with increasing convex hull size.

Foremost, it is clear that the localization error increases with increasing transmitter-receiver distance, as well as with decreasing ULB power. This is due to the increasing range estimation error, which subsequently affects the computed source position. Another straightforward observation is that the TOA method offers much greater accuracy than its TDOA equivalent. This is well patented by the y axis scale in Fig. 19. It is ergo the recommended source localization methodology

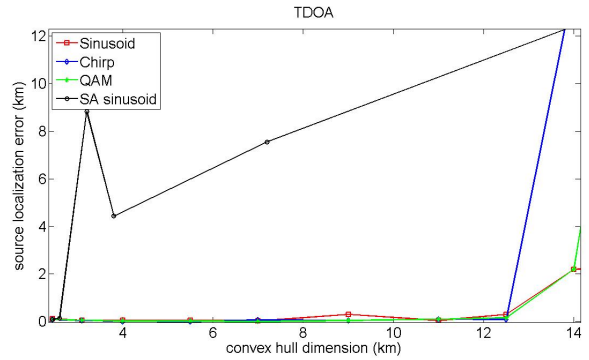


Fig. 20. TDOA source localization error as a function of the dimension of the receiving convex hull (topology 2), zoomed at the lower convex hull sizes for which the TDOA source localization error is very small when the alternative signals are employed.

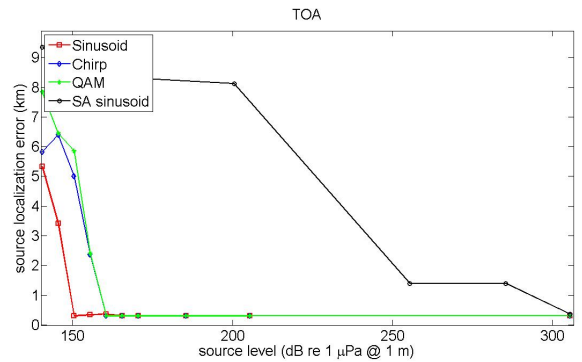


Fig. 21. TOA source localization error as a function of the transmitter's source level (topology 3). There is a decrease of the TOA source localization error with increasing ULB power.

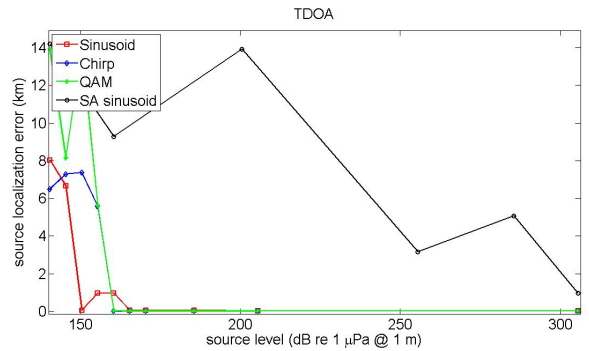


Fig. 22. TDOA source localization error as a function of the transmitter's source level (topology 3). There is a decrease of the TDOA source localization error with increasing ULB power.

for this type of problems, if transmit schedules are perfectly known.

Regarding Figs. 18 to 20, once the ocean noise begins dominating the range estimation process, the localization algorithms become erratic. That is, since they are given very noisy range estimates, their output is also nearly random. Hence, if we perform the same simulation repeatedly, with all the same conditions, the output of the TOA and the TDOA algorithms

will diverge. That explains the non-logical evolution of the localization errors with the highest convex hull sizes (from 3 km, in the SA sine case, and from 13 km for the remaining signals).

Still referring to Figs. 18 to 20, we observe that for a convex hull size not bigger than approximately 14 km, the localization error is less than 500 m when the TOA algorithm and the alternative signals are employed. The SA signal performs much worse, only guaranteeing a good source's position estimate for convex hull dimensions under 3 km. The TDOA technique is seen to provide fairly good estimates up to a convex hull dimension of approximately 13 km for the alternative signals, and 2.5 km for the state of the art.

Concerning Figs. 21 and 22, it is observed that the localization-error evolution with ULB power is an asymptotic function, which means that there is a set of transmitter acoustic powers for which the best performance is achieved. The minimum of these values is approximately 165 dB re $1\mu\text{Pa}@1\text{m}$ for the alternative signals, and source localization in the SA case is only successful for $SL = 305\text{ dB re }1\mu\text{Pa}@1\text{m}$, approximately.

Even though our simulations do not cover the possibility of transmitting a digital message containing information such as the FDR depth, that could easily be used to confirm our localization estimates, regarding the z coordinate.

VI. CONCLUSION

The main contributions of this paper were presented in Section V. Subsection V-B proved that the state-of-the-art system is inadequate when the distance separating the ULB from the hydrophones is too large, as the ULB signal's high frequency prevents propagation to long ranges due to high path losses. Additionally, it was verified that the proposed alternatives allow an increase of approximately 10 km on the maximum range for which signal detection is accomplished. In this sense, the sinusoid outperformed the other signals because its receiver's bandpass filter has a narrower bandwidth. Furthermore, Subsection V-C allowed us to compare the implemented TOA and TDOA algorithms, clearly demonstrating that the range-based methodology is naturally more accurate than its range-difference-based counterpart. That is due to the TDOA susceptibility to the measurements accuracy, as this algorithm depends on very subtle delay-differences between sensors. The standardized source level of 160.5 dB re $1\mu\text{Pa}@1\text{m}$ permits a correct source localization for a maximum convex hull dimension of approximately 3 km and 14 km for the SA sine and the proposed alternatives, respectively, when the TOA technique is used; these values decrease to 2.5 km and 13 km in the TDOA case. It was also seen that an increase of the ULB's source level is advantageous, as the localization error decreased with increasing ULB power. We also found that the source localization algorithms work better if the source lies inside the convex hull; this finding is corroborated by several authors who study range-based localization.

In conclusion, we propose a frequency decrease of the ULB transmitted acoustic signal. Likewise, employing the TOA

algorithm to yield the source's position is strongly advised. This obviously implies that the ULB must function as a transponder.

REFERENCES

- [1] Dale Green. Recovering Data and Voice Recorders Following At-Sea Crashes. In *Oceans 2010 IEEE – Sydney*, May 2010.
- [2] Flight Data Recover Working Group. Technical report, BEA, 2009.
- [3] Steven M. Shope. Spread spectrum underwater location beacon system. *United States Patent*, August 1990.
- [4] Finn B. Jensen, William A. Kuperman, Michael B. Porter and Henrik Schmidt. *Computational Ocean Acoustics*, chapter 1. Springer, 1994.
- [5] David Brady and James C. Preisig. *Wireless Communications: Signal Processing Perspectives*, chapter 8. Prentice Hall, 1998.
- [6] Steven M. Kay. *Fundamentals of Statistical Signal Processing*, volume 2: Detection Theory. Prentice Hall, February 1998.
- [7] Milica Stojanovic. On the Relationship Between Capacity and Distance in an Underwater Acoustic Communication Channel. In *WUWNet '06 Proceedings of the 1st ACM international workshop on Underwater networks*, September 2006.
- [8] Michael B. Porter. The kraken normal mode program. Technical report, SACLANT Undersea Research Centre, October 1995.
- [9] World ocean system (woss) library. Technical report, World Ocean System, August 2010.
- [10] Amir Beck, Petre Stoica and Jian Li. Exact and approximate solutions of source localization problems. *IEEE Transactions on Signal Processing*, 56(5), May 2008.
- [11] Acoustic toolbox. <http://oalib.hlsresearch.com/>.
- [12] Orlando Camargo Rodriguez. General description of the BELLHOP ray tracing program. Technical report, Physics Department, Signal Processing Laboratory, Faculdade de Ciências e Tecnologia, Universidade do Algarve, June 2008.
- [13] John Proakis and Masoud Salehi. *Digital Communications*. McGraw-Hill Science/Engineering/Math, 5 edition, November 2007.